Automotive Aerodynamics Sensing Using Low-profile Pressure Sensor Strip

Dayi Zhang, Senthilkumar Subramanian, Rory Hampson, William Jackson, Konstantinos Kontis, Gordon Dobie, Charles Macleod

Abstract—**Measuring aerodynamics is crucial in the automotive industry as it helps engineers to optimise designs to improve vehicles' stability and performance. Pressure sensors are widely used to measure aerodynamics. The sensors measure the pressure differences around the vehicle, as well as the pressure distribution around it. These measurements can help to determine the aerodynamic drag and lift forces acting upon the vehicle. However, traditional sensors are relatively large and can be intrusive, making them difficult to integrate into a vehicle's design. Computational Fluid Dynamics (CFD) offers a low-cost option into gathering representative pressure data, the results may be limited by the mathematic model used and other factors which often require a high level of skill to use adequately. This paper presents a novel miniature, low profile aerodynamic sensor strip for use in the automotive sector. The sensor strip is significantly smaller than conventional pressure sensors, while maintaining high levels of accuracy and precision. The compact design of the sensor strip allows for easy deployment on existing cars, and its small size minimizes the effect on the aerodynamic drag of the vehicle. The sensor's miniature size and good performance make it a promising solution for automotive applications, such as active aerodynamic control systems. The sensor has been thoroughly tested in a wind tunnel and has been shown to accurately measure air pressure. Particle image velocimetry results showed the sensor's impact on the airflow was below 4%. An empirical pressure measurement on a passenger car demonstrated a successful implementation in the field.**

Index Terms—**Low-profile pressure sensor strip; Automotive pressure measurements**

I. INTRODUCTION

AUTOMOTIVE aerodynamic sensing and measuring has become ever more popular in recent years. It helps engineers to understand the aerodynamics and optimise designs to improve the vehicles' stability and performance. State-of-the-art methods for aerodynamic sensing include Particle Image Velocimetry (PIV) systems, Computational Fluid Dynamics (CFD) simulations, as well as pressure sensors.

Particle Image Velocimetry (PIV) is a flow visualisation technique used in fluid patterns to measure the velocity of fluid flow. It seeds a fluid with small tracer particles, illuminating the fluid, capturing images of the particles, and then analysing

the images to determine the particles movement in the fluid. [1] studied aerodynamic characteristics of a vehicle model using PIV and CFD methods to measure the near wake flow structure. A. Parfett et al. [2] used PIV to obtain instantaneous records of the velocity field around an F1 car wheel and described the flow about a smooth wheel rolling along a plane surface. Although PIV is useful in aerodynamic analysis, it also has many drawbacks. PIV requires many images to estimate velocities, which requires high computational resources. The presence of particles can alter the fluid properties and affect the accuracy.

Computational Fluid Dynamics (CFD) is a computer-based simulation method. It uses mathematical models to numerically analyse and predict fluid flow. D. Martins et al. [3] utilised a Detached-Eddy Simulation CFD approach to analysis the aerodynamic interactions between a three-element wing and wheel in ground effect on an F1 car. Similarly, D. Patel et al.[4] used a CFD simulation to demonstrate the impact of a race car front wing on aerodynamic performance when cornering. The simulation was validated against PIV results. K. Kurec et al. [5] utilised a CFD simulation and a scale model to study a moving spoiler, showing in a significant change of car downforce. CFD has several disadvantages including high computational cost, expert knowledge in modelling and set-up, as well as potential limitations in creating accurate representations of complex geometries in the case the user may not have access to the original designs.

Pressure sensors are also used in automotive industries to optimize the vehicle's performance by measuring the pressure around it. Engineers uses these sensors to measure the pressure difference between the front and rear, top and bottom to adjust car parameters such as wing angles to improve the car's aerodynamic efficiency and stability during high-speed driving. F. Cogotti et al. [6] built two reference cars to compare the pressure distribution on the vehicle surface. The reference cars have hundreds of pressure ports distributed on the car surface to measure the surface pressures. The reference cars provide a better understanding of the aerodynamic differences between the road and development tools. Similar applications are seen in [7], [8], using pressure sensors to measure air flow on car surfaces. T. Polonelli et al. [9] utilised pressure sensors for aerodynamic and aeroacoustics monitoring on wind turbines. F. Robertson et al. [10] made eight scaled models of lorries and placed pressure sensors inside these models to investigate aerodynamic flows created when travelling in a long convoy. Similarly, [11], [12] used large pressure sensors to measure aerodynamic changes on railway trains.

In the aforementioned literature, measuring aerodynamics

using pressure sensors requires the destructive drilling of ports into the surface of the component being tested, to prevent these bulky sensors from altering the fluid properties. However, the component is no longer suitable for its original purpose after testing concludes. Therefore, scaled reference models were utilised for aerodynamic pressure measurements, while bulky pressure sensors can be fitted inside the models [5], [6], [10], [11]. Such methods require precise modelling to ensure that the scaled models accurately match their full-sized counterparts. In [13], the authors present a wireless pressure measurement system to estimate aircraft airspeed by acquiring the pressure over the wing surface. The sensors are low-profile and significantly smaller than those described in the literature. However, the system is made by rigid printed circuit boards and only consists of two sensors, which makes it difficult to measure 3D pressure distributions on the leading edge of the wing.

The pressure sensor setup becomes further complicated by the need to connect these ports via a network of tubes to the pressure-measuring instrument. This procedure can become very labour-intensive when applied to intricately formed models and valuable components such as the front wings of Formula 1 cars [14] and the wings of modern fighter aircraft, especially when the components are small and have complex geometry [15].

II. AIM AND OBJECTIVES

Aerodynamic measurements using PIV require high computational resources to process captured images and estimate velocities. Similarly, CFD requires a high computational cost, expert knowledge in modelling, and set-up. The state-of-the-art measurement instruments described in the literature are relatively bulky and require drilling pressure taps into the surface, making them unsuitable for non-destructive and in-situ aerodynamic measurements.

This project aims to create and validate a rapidly-deployable, non-invasive sensor for measuring pressure, making the development of aerodynamic systems simpler and more cost-effective, reducing the complexity and high cost of pressure measurement in fluid dynamics research. The paper proposes a sensor strip consisting of multiple pressure sensing elements that can be temporarily applied to any complex 3D body without altering or damaging the material surface.

The overview and technical specifications of the sensor are discussed in Section III. In Section IV, the accuracy of the sensor is characterised and compared to conventional pressure sensors in laboratory setups, including a 2D cylinder and a 3D S-duct. Section V presents the impact of the sensor thickness on air flow using PIV imaging. An empirical pressure measurement is demonstrated on a passenger car in Section VI and results are compared to CFD simulations.

The main contributions of this paper are:
- Development of a low-profile sensor strip to measure aerodynamic pressure for non-destructive automotive applications.
- Evaluation of the sensor accuracies in laboratory 2D cylinder and 3D S-duct.

- Investigated the impact of the sensor thickness on the air flow using Particle Image Velocimetry.
- Demonstrated the sensor application in an empirical pressure measurement on a passenger car.

III. SENSOR OVERVIEW AND SPECIFICATIONS

The sensor strip is made up of 12 MEMS nano pressure sensors and a microcontroller serving as a data accumulator and sensor controller. The pressure sensors and microcontroller are integrated on a 0.1mm flexible printed circuit board to minimize thickness and provide flexibility to reduce the bend radius. The sensor can bend with a radius larger than 5 mm, allowing it to conform to complex geometries and multi-axial curvatures inherent in many aerodynamic systems. This makes the system suitable for a wide range of applications.

The pressure sensing element is an ultra-compact piezoresistive absolute pressure sensor, featuring factory calibration and embedded temperature compensation.

The microcontroller (with a custom firmware, written in C) communicates with the sensors using the SPI protocol. It initializes the sensor readings, collects the pressure data from each element, and repackages the data to send to the DAQ controller.

The sensor strip is connected to a USB powered, U400 DAQ controller from PPS [16], which streams the pressure data to a computer at a maximum rate of 200 Hz via a USB cable (as shown in Fig. 1).
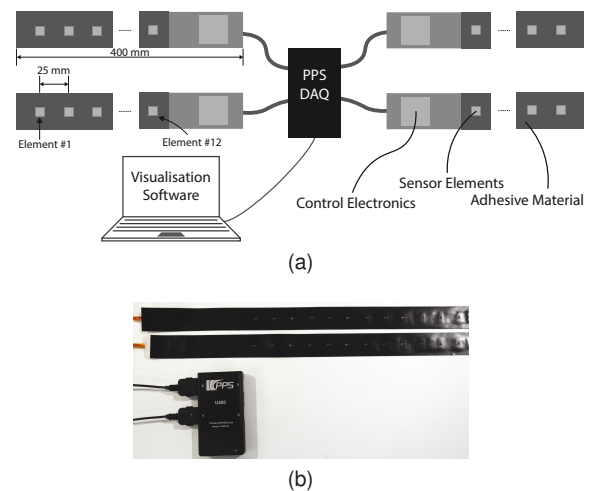

Fig. 1. (a) Working schematic of an integrated sensor system. (b) Four wired sensors are connected to PPS U400 DAQ controller, communicating with a GUI and recorder on a computer.
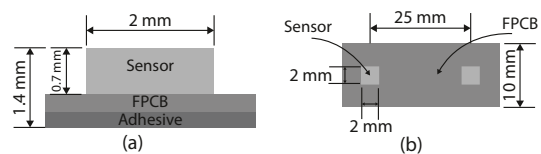

Fig. 2. Sensor dimensions (a) side view (b) top view

Up to four sensor strips can be connected to the DAQ controller and used individually in four different regions of the structure being tested. The sensors can also be joined into

TABLE I
THE SENSOR STRIPS TECHNICAL SPECIFICATIONS

Measurement Range (Absolute Pressure)	26-126 kPa
Resolution	1/40960 kPa
Sample Rate	200 Hz
No. Elements	12
Element Pitch	25 mm
Sensor Strip Length	400 mm
Sensor Width	10 mm
Total Thickness	1.4 mm

a large array to map pressure in a larger area. Low-profile cables are used to prevent interference with measurements. The sensor's technical specifications are listed in Table I, and its dimensions are shown in Fig. 2.

The sensor strip pitch is defined by subtracting the reservations for the electronic regions ($L_{electronics}$) from the maximum length of the flexible PCB that the manufacturer can produce (L_{max}), and then evenly distributing it among the number of sensing elements (n), as (1). These parameters can be adjusted based on different design requirements. Herein, the maximum length is 400 mm, the electronic region reserves 100 mm, and the strip contains 12 elements. Therefore, the pitch is 25 mm.

$$pitch = \frac{L_{max} - L_{electronics}}{n} \qquad (1)$$

IV. SENSOR ACCURACY CHARACTERISATION

The effectiveness and accuracy of the sensor were verified through two sets of experiments under different flow conditions.

In the first experiment, the sensors were placed on the external surface of a 2D cylinder to measure external flow pressure, which was then compared to the reference values. In the second experiment, the sensors were placed inside an S-duct to measure internal flow pressure, which was also compared to the reference values.

A Scanivalve ZOC 23b pressure scanner [17] was used as the reference sensor to provide accurate pressure measurements. These Scanivalve sensors were installed underneath the cylinder and S-duct and measuring the pressures through the drilled taps.

A. External flow around a 2D Cylinder

The experiment was designed to compare the pressure at different areas of the flow field (stagnation, transition, and wake areas) around a stationary cylinder. The 160 mm diameter 2D cylinder was fixed vertically inside a 2.1 m × 1.5 m closed-circuit Handley-Page wind tunnel. The simple and effective aerodynamic model, similar to this, was presented in [18].

The tunnel was operated at flow rates of 11.6, 16.2, and 21.1 m/s, and the sensor strips were positioned such that the first and tenth sensor elements corresponded to the front and rear stagnation points respectively, and the fifth sensor element coincided with the cylinder's 90° point, as shown in Fig. 3.

Fig. 4 shows good alignments between the ground truth sensor and the sensor strip readings at the three flow rates. The
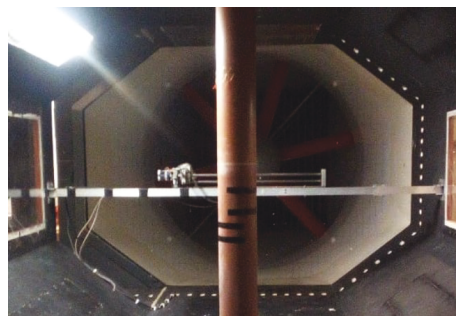

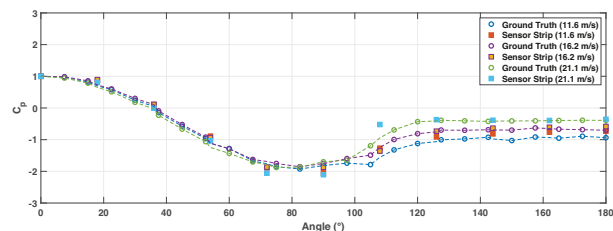Fig. 3. Experiment setup for external flow measurement on 2D cylinder

Fig. 4. Comparison of C_p (Pressure Coefficient) distribution around the cylinder.

average difference between the measured pressure coefficient from the sensor and the ground truth value was 0.059.

B. Internal flow through a 3D S-duct

The S-duct rig provides a controlled experimental environment to study the pressure distribution within the duct, the pressure taps and Scanivalve pressure sensors allow for accurate measurements of the ground truth pressures. The complex geometry of the S-duct adds to the realism of the experimental setup and provides a challenging environment to validate the pressure readings obtained from the sensor strip. As Fig. 5, the pressure taps were located at equiangular spacings of 0°, 60°, 120° and 180°. The S-duct contains four rows of pressure taps at these four angles, with each row having 12 pressure taps. Each pressure tap is connected to a Scanivalve sensor. Therefore, the S-duct has a total of 48 Scanivalve sensors. The duct both ends were connected to a straight section (inlet and outlet) to help developing the boundary layer at the inlet and to align the flow to the fan at the exit [19], [20]. The exit of the duct was connected to a 2-stage axial fan to control the flow velocity (18, 22 and 27 m/s).
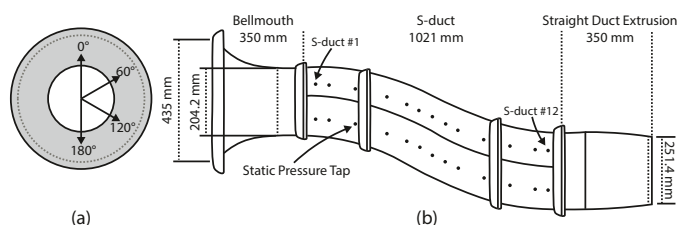

Fig. 5. (a) Front cross-section showing the streamwise location of static pressure taps. (b) S-duct assembly with static pressure taps.

The sensor strips were positioned to align with the static pressure taps along the inside walls of the S-duct, as shown in Fig. 6. A single sensor strip can cover approximately 300 mm, while the S-duct length is around 1000 mm. The single strip was able to cover approximately 30% of the total duct length, requiring twelve sensor strips to cover the same area as the original 48 Scanivalve sensors. As shown in Fig. 1, four sensor strips are connected to the DAQ controller, and the experiments were repeated three times by placing the strips in different locations.
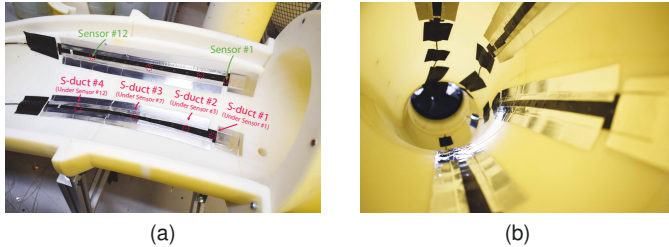

(a)   (b)

Fig. 6. Sensors placed inside the S-duct and coincide with the static pressure taps.

The comparisons between the sensor strips and the ground truth with three velocities are shown in Fig. 7. As shown in Fig. 7(a), the sensor mounted in the top wall (0°) corresponds well with the Scanivalve readings. The sensor successfully measured the low pressure at the entrance of the duct, and the high-pressure region through the bends of the diffuser [21]. Similar to the 2D cylinder experiment result, small variation in the sensor output has been observed when the flow is parallel to the sensor strip.

The static pressure distribution at 60°, 120°and 180° show the similar results. The pressure measurements from the sensor strips at different flow velocities are consistently aligned with the Scanivalve pressures. The average difference between the Scanivalve readings and the sensor strip measurements were 0.092 ‰.

Overall, the experiments result of the 2D cylinder and 3D S-duct shows the accuracy of the sensor strip is well matched with the ground truth pressure measurements at stagnation points, wake region and other curved surfaces.

V. PIV INVESTIGATION ON SENSOR SURFACE

Although the sensor is low-profile (1.4 mm), it was suspected that the thickness, especially the small increment at the tip of sensing elements would moderately impact the air flow. Therefore, a Particle Image Velocimetry (PIV) was performed on the sensor strip to quantify the impact of the sensor thickness on the flow parallel to the flat plate surface boundary layer using a purpose-built setup, as shown in Fig. 8. The experiment setup is adopted to fit the sensor strip in this paper, based on the Andreou's design [22]. The setup includes a plenum chamber and a laser PIV imaging system. The chamber is pressurised 4% above the atmosphere and filled with oleic acid particles for PIV imaging. The plenum chamber output is a 16.76 mm exit diameter nozzle, specially designed to expel a uniform flow, to discharge pressurised air into the region and create jet flow with oleic acid particles above the sensor. The jet flow and particles velocities are controlled by tuning the chamber pressure using valves, as Fig. 8. In this experiment, the jet flow velocities are 16, 55 and 84 m/s, corresponding to Reynolds number 1.81×10^4, 6.2×10^4, and 9.51×10^4. The pressures inside the chamber to create these velocities are 5, 18 and 45 psi, respectively.

The sensor strip was mounted on a flat plate and placed at the near field flow development jet boundary region. A Litron LDY301 YLF [23] outputs laser beams at 500 Hz, passing through glass fibres and giving the rise to the laser sheet in the sensing region. The laser sheet is parallel to the nozzle exit plane and illuminates the particles. A Photron APX-RS high-speed camera [24] is used to capture these illuminated particles at 1000 fps. A Tokina 35-105mm telephoto lens [25] was used to observe the fine details of the change in flow characteristics brought on by the presence of sensors. A
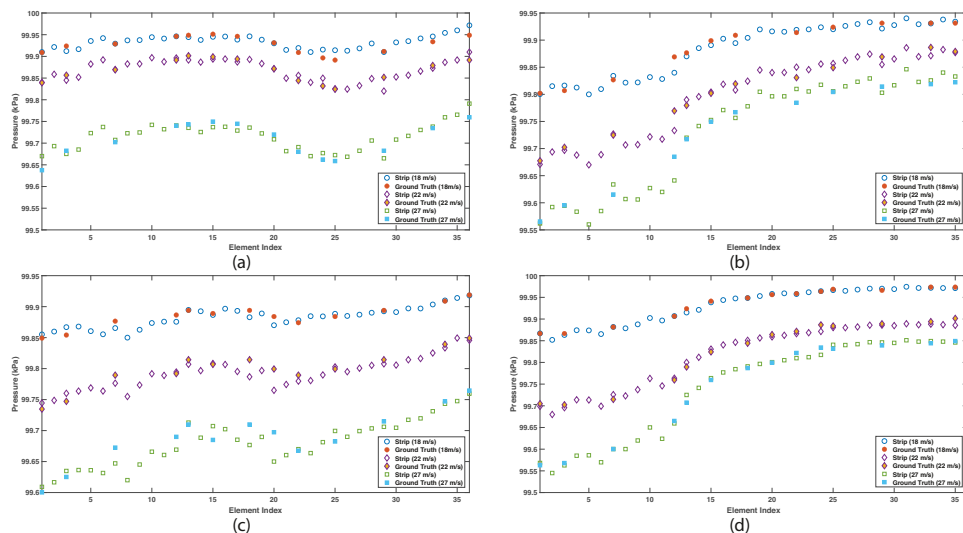

Fig. 7. Comparison of streamwise static pressure variation along (a) 0° axis (b) 60° axis (c) 120° axis (d) 180° axis (from inlet (left) to outlet (right))
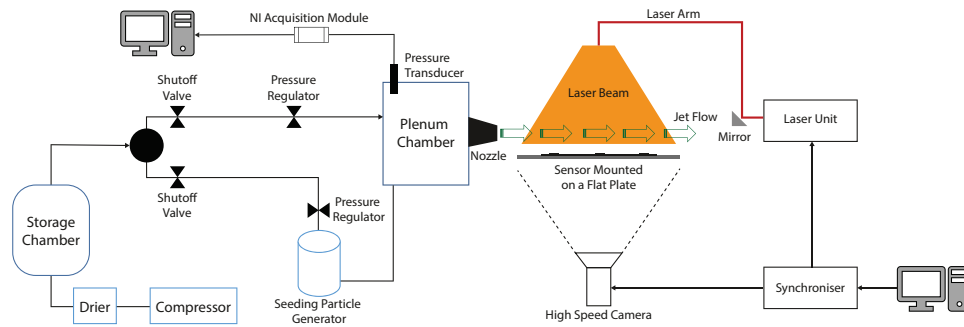
Fig. 8. PIV Experiment Setup

LaserPulse Synchronizer 610035 [26] synchronises the laser generator and the camera shutter.

For comparison, data sets were acquired without the sensor strip to provide the jet flow pattern in the absence of the sensor strip.

PIV images gathered with and without the sensor strip are shown in Fig. 9. The jet flow velocity magnitude, extracted from the PIV images are shown in Fig. 10. The values are taken at 3 different standoff (1, 2 and 4 mm) above the sensor surface. The acceleration of flow over the elements and streamwise velocity component disturbance as well as the element pitch (25 mm) are observable in the Fig. 9 (b), (d) and (f). The sensing element is like a mini hump in the flow path. The humps produce a local velocity variation. As shown in Fig. 9 and Fig. 10, the particle experiences an incremental increase in velocity when it passes the middle of the hump and slows down when it reaches the troughs between two humps.

This flow characteristics change occurs when the wall disturbance is more severe, causing increased shear stress on the crest [27], [28], [29] presents an unfavourable pressure gradient in the presence of a hump structure, which causes the flow turbulences near the surface. However, as shown in Fig. 9 (b), (d) and (f), owing to the low thickness, the sensor does not create such flow turbulences. The flows across the sensor strip and near of sensing elements are smooth and stable. As presented in Fig. 10, the velocity variations near the sensing elements are significantly diminished when the standoff is larger than 4 mm.

Fig. 11 illustrates the velocity distributions relatively close to the surface (1 mm above the sensor) in percentage. It shows the peak changes due to the presence of the sensing elements are similar at three velocities and the variances are less than 4% of the velocity without the sensor.
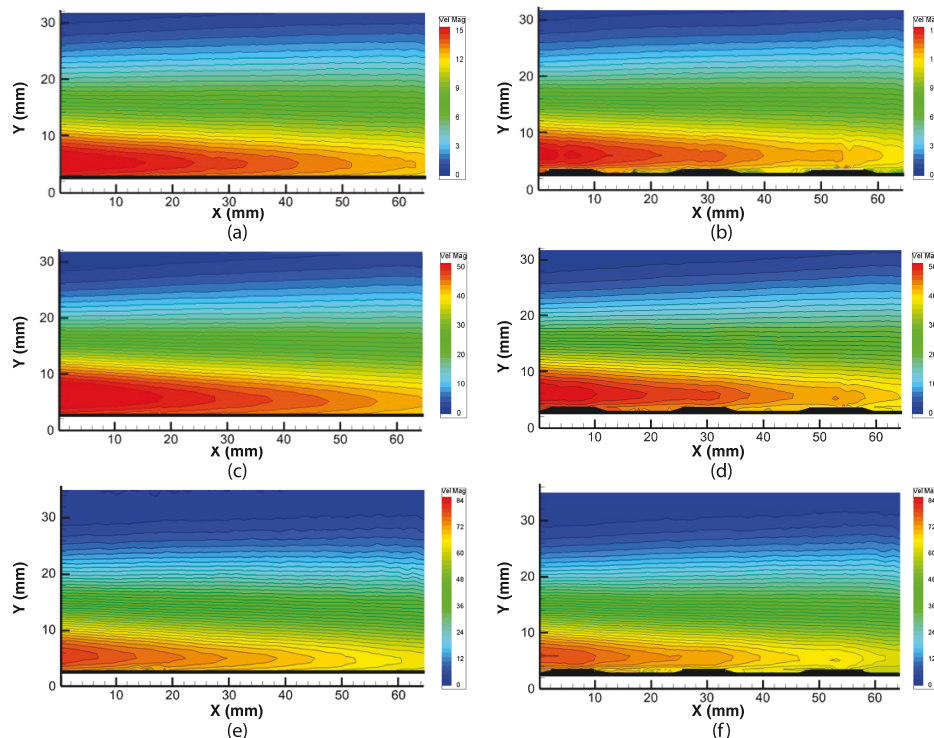

Fig. 9. Close-up view of streamwise velocity distribution along X axis over a flat plate at various speeds. (a) and (b) are 16 m/s, (c) and (d) are 52 m/s, (e) and (f) are 84 m/s. (a), (c) and (e) are captured in the absence of the sensor. (b), (d) and (f) are captured with the sensor.
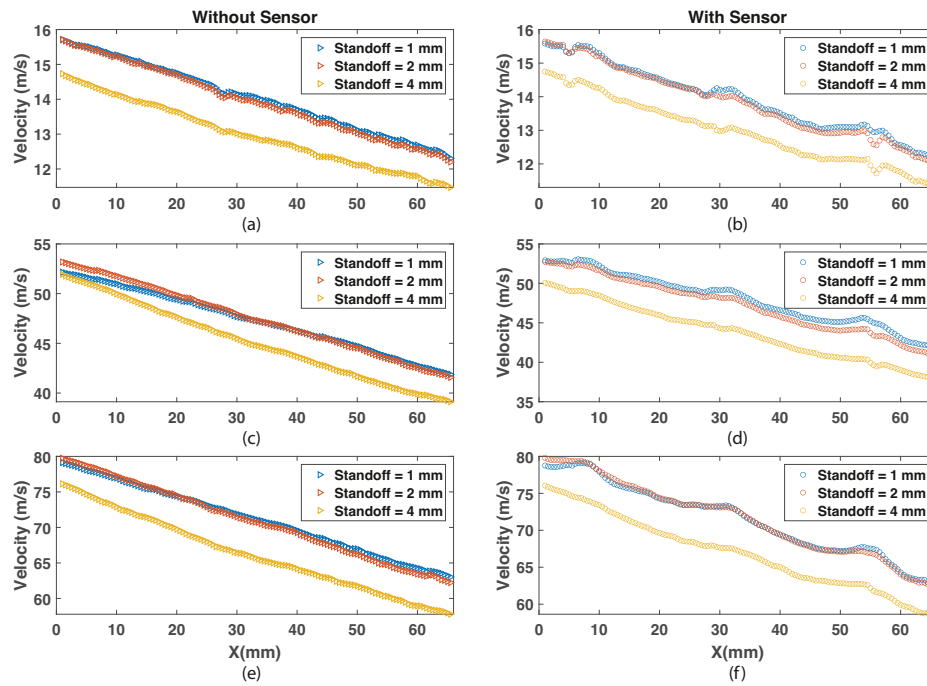
Fig. 10. Comparison of streamwise velocity magnitude at vertical distance of 1, 2 and 4 mm from surface at various speeds. (a) and (b) are 16 m/s, (c) and (d) are 52 m/s, (e) and (f) are 84 m/s. (a), (c) and (e) are captured in the absence of the sensor. (b), (d) and (f) are captured with the sensor.
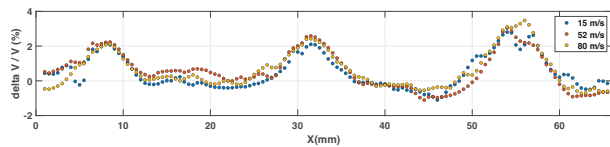

Fig. 11. Percentage change in velocity due to sensor thickness in parallel flow at 1 mm from sensor surface

VI. PRACTICAL CAR PRESSURE MEASUREMENTS

A. Experiment Setup

The sensor was tested by conducting empirical pressure measurements on a passenger car. The sensor readings were compared to ground truth values from a two-dimensional Computational Fluid Dynamics (CFD). As Fig. 12, the sensor strips were mounted on the surface of a Volkswagen MK7 Golf and the car was driven on smooth roads at various speeds (up to 99 km/h) lasting around one hour. One sensor strip was placed inside the car to record pressure variations due to altitude changes, with the readings from the other strips subtracted to compensate for altitude impacts.

To prevent pressure value drift due to crosswind, the experiment was conducted on a quiet, dry day with low wind velocity. The strips were placed as close to the axial centre of the vehicle as possible to minimize measurement inaccuracies caused by the tangential component of wind pressure.

B. Real-time Pressure Monitoring Software

The PPS U400 DAQ collects sensor data at a rate of 200 Hz and streams to a computer. A custom interface software, written in C#, was created using the PPS Chameleon DLL
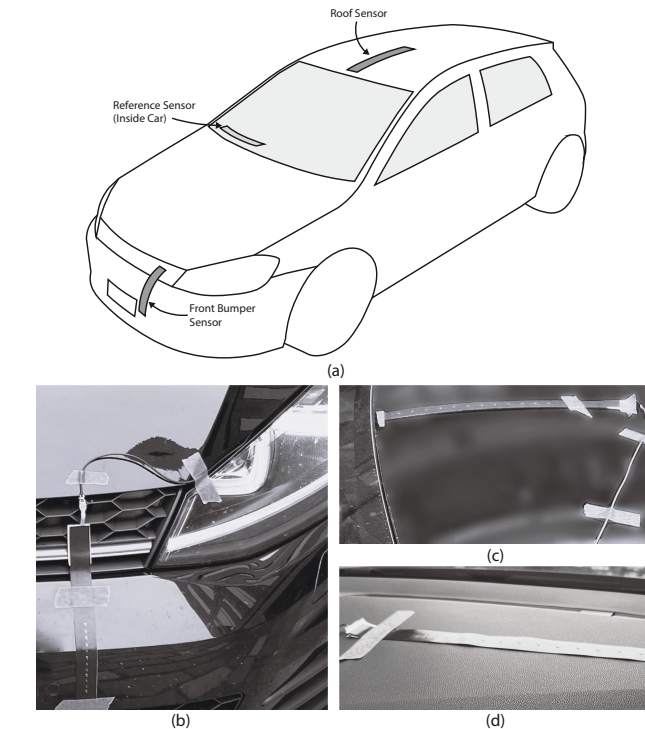

Fig. 12. Experiment setup on a passenger car. (a) location diagram (b) front bumper (c) roof (d) inside the car.

[16] to communicate with the U400 DAQ controller through the USB.

The software visualises the pressure readings in real-time, as presented in Fig. 13. The arrows in the figure represent the pressure measured by each element of each sensing strip,

with the length and colour indicating the pressure amplitude and the orientation indicating the pressure direction. Additionally, the average internal pressure is subtracted from each external element for display display. Captured data, recorded by the software, are exported to CSV format file for use in offline analysis. A synchronised video was recorded during the experiment to correlate the pressure readings with the car speedometer values.
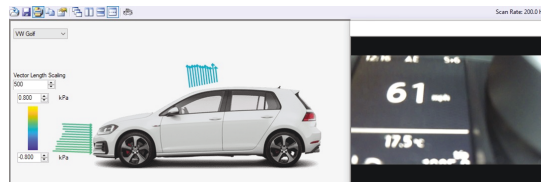

Fig. 13. Screenshot of the graphical user interface of real-time pressure visualisation and monitoring with the car at 98 km/h (61 miles per hour, as shown from synchronised video) with the cabin pressure subtracted to show relative pressures.

C. Computational Fluid Dynamics Simulation

In this experiment, traditional pressure measuring methods (drilling taps into the cylinder and S-duct and placing sensors underneath) described in Section IV and V are not applicable due to the inaccessible area under the surface and the resulting damage to the car after testing.

As a result, a computational fluid dynamics (CFD) simulation was used as the ground truth reference. The simulation was conducted using 2D Reynolds averaged Navier-Stokes (RANS) simulations in the STAR-CCM+ software [30]. Six-speed settings – 34 km/h, 48 km/h, 63 km/h, 79 km/h, 86 km/h, and 99 km/h were considered in the simulation.

The fluid is expelled from the 2D inlet into a rectangular domain and a fine rectangular grid mesh with a base size of 10 cm was created to provide sufficient resolution around the car shape. The results were generated using an incompressible flow model in Star-CCM+. The k-ε turbulence model was chosen as it has been shown to perform well in predicting turbulent flows in previous studies [31], [32], [33].

Fig. 14 shows the computed pressure distribution around the car at a speed of 86 km/h. The simulation accurately depicts a suction zone at the start of the rooftop and a high-pressure region at the front bumper.
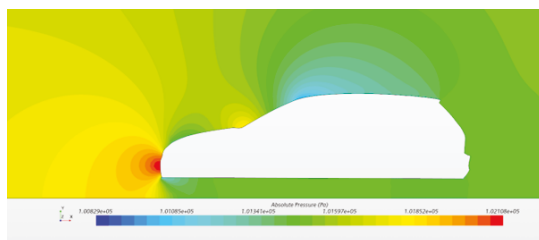

Fig. 14. Simulated pressure distribution for velocity at 86 km/h.

D. Results and Discussion

Fig. 15 and Fig. 16 present the comparison between the sensor strip measurements and ground truth references for di

fferent velocities, data was captured at speeds up to 99 km/h, the data shown here is a selection from on road trials.
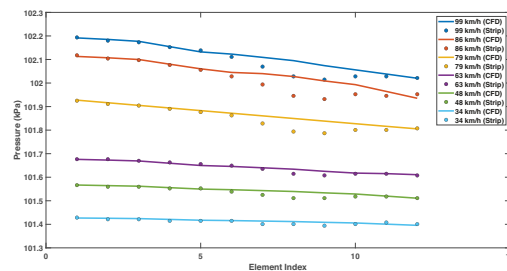

Fig. 15. Comparison of computer simulated pressures with the sensor located at the front bumper (where element 0 is at the bottom of the bumper, and 11 at the top).
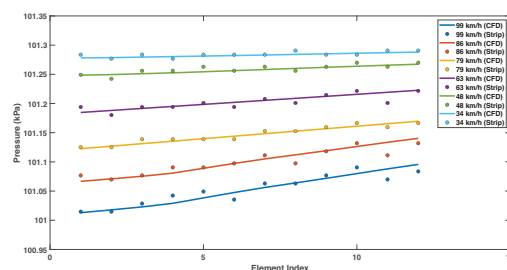

Fig. 16. Comparison of computer simulated pressures with the sensor located on the roof (where element 0 is towards the front and 11 towards the rear).

The ground truth data were obtained from the CFD simulation model at the same locations as the sensor strips were placed. Similar to the conclusions in Section IV and V, the CFD results are in good agreement with the sensor strip measurements for the roof region of the car.

With the increment of the car velocity, the pressure increased at the car front bumper and decreased on the roof, as expected from the CFD simulation results, and observed by the sensor measurements.

In general, the front bumper readings from the first 6 elements and the values from 7 to 11 at low speeds are aligned well with the CFD results. The reading from element 7 to 11 are located at the curved section of the front bumper, which is also the location of the car's stagnation region. The 3D geometry at this area is relatively complicated and the simulation model does not perfectly match the car in this region. As a result, the readings from these elements slightly mismatched the CFD simulations at the high speed.

The computed pressure values on the roof were compared with the sensor strip measurements and there was good agreement at lower speeds. There was a small discrepancy at higher speeds due to the 3D flow characteristics of the car and the presence of additional parts such as wipers ahead of the front screen in the real car.

The mean difference between the CFD simulation and sensor strip measurements are 0.012 ‰ on the vehicle roof section and 0.032 ‰ on the more complicated car front bumper area.

VII. CONCLUSION

This paper presents a pressure sensor strip designed for automotive aerodynamic measurement. The accuracy of the sensor was characterized and validated in laboratory environments using a 2D cylinder and a 3D S-duct.

The 3D S-duct trials showed the sensor to be within 0.1 ‰ of a commercially available Scanivalve system. In a case study of dynamic measurement compared to 2D CFD results, a mean difference of 0.012 ‰ on the vehicle roof section and 0.032 ‰ front bumper area was observed. The results of the sensor readings were found to be well aligned with measurements from conventional, ground-truth pressure sensors.

A particle image velocimetry (PIV) investigation was conducted and showed that the impact of the sensor's thickness on the airflow was below 4%. The sensor was also mounted on a passenger car and underwent an empirical experiment trial. The results of the trial were also well aligned with computer simulations, indicating that the sensor can accurately measure pressure on automobiles in practical scenarios.

The sensor can also be deployed onto more application-specific structures, particularly in aerospace and automotive design [34] where the straightforward and non-invasive nature of the sensor can have the greatest impact. Furthermore, the sensor can replace the methodologies presented in the literature for measuring aerodynamics in other applications, such as wind turbines [9] and aircraft modelling [13]. In applications that involve measuring larger surface areas, such as modelling lorries or trains [10], [11], [12], multiple sensor strips can be connected to cover more space. Alternatively, the sensing elements can be rearranged into a 2D array instead of a long strip, which would increase the coverage in two dimensions.

The current pitch of the sensing elements is 25 mm. To improve its suitability for use in high-pressure gradient environments like flow over aerofoil leading edges, it has been proposed to reduce the pitch for increased spatial resolution. Future work will aim to optimize the system, including increasing the number of sensors connected to the computer and making the system wireless.

ACKNOWLEDGMENT

CREDIT AUTHOR STATEMENT

Dayi Zhang, Rory Hampson: sensor design, writing—original draft preparation, review and editing; **Senthilkumar Subramanian**: Writing—original draft preparation, data collection; formal analysis; **William Jackson**: Software, writing— review and editing; **Konstantinos Kontis, Gordon Dobie, Charles Macleod**: Supervision, Funding acquisition.

REFERENCES

[1] Y. Zhang, J. Zhang, K. Wu, Z. Wang, and Z. Zhang, "Aerodynamic characteristics of mira fastback model in experiment and cfd," *International Journal of Automotive Technology*, vol. 20, pp. 723–737, 2019.

[2] A. Parfett, H. Babinsky, and J. K. Harvey, "A study of the time-resolved structure of the vortices shed into the wake of an isolated f1 car wheel," *Experiments in Fluids*, vol. 63, 2022.

[3] D. Martins, J. Correia, and A. Silva, "The influence of front wing pressure distribution on wheel wake aerodynamics of a f1 car," *Energies*, vol. 14, 2021.

[4] D. Patel, A. Garmory, and M. Passmore, "The effect of cornering on the aerodynamics of a multi-element wing in ground effect," *Fluids*, vol. 6, 2021.

[5] K. Kurec, M. Remer, T. Mayer, S. Tudruj, and J. Piechna, "Flow control for a car-mounted rear wing," *International Journal of Mechanical Sciences*, vol. 152, pp. 384–399, 3 2019.

[6] F. Cogotti, M. Pfadenhauer, and T. Wiegand, "Potential of porsche reference cars for aerodynamic development," *Progress in Vehicle Aerodynamics and Thermal Management*, pp. 216–237, 2018.

[7] J. Haff, S. Lange, T. Barth, and H. Wilhelmi, *Progress in Vehicle Aerodynamics and Thermal Management*, 2018.

[8] G. Pavia and M. Passmore, "Characterisation of wake bi-stability for a square-back geometry with rotating wheels," *Progress in Vehicle Aerodynamics and Thermal Management*, pp. 93–109, 2018.

[9] T. Polonelli, H. Muller, W. Kong, R. Fischer, L. Benini, and M. Magno, "Aerosense: A self-sustainable and long-range bluetooth wireless sensor node for aerodynamic and aeroacoustic monitoring on wind turbines," *IEEE Sensors Journal*, vol. 23, pp. 715–723, 1 2023. [Online]. Available: https://ieeexplore.ieee.org/document/9967940/

[10] F. H. Robertson, F. Bourriez, M. He, D. Soper, C. Baker, H. Hemida, and M. Sterling, "An experimental investigation of the aerodynamic flows created by lorries travelling in a long platoon," *Journal of Wind Engineering and Industrial Aerodynamics*, vol. 193, p. 103966, 10 2019.

[11] C. J. Baker and M. Sterling, "Aerodynamic forces on multiple unit trains in cross winds," *Journal of Fluids Engineering*, vol. 131, 10 2009.

[12] H. Gao, T. Liu, H. Gu, Z. Jiang, X. Huo, Y. Xia, and Z. Chen, "Full-scale tests of unsteady aerodynamic loads and pressure distribution on fast trains in crosswinds," *Measurement*, vol. 186, p. 110152, 12 2021.

[13] J. P. Leitzke, A. D. Mea, L.-M. Faller, S. Mühlbacher-Karrer, and H. Zangl, "Wireless differential pressure measurement for aircraft," *Measurement*, vol. 122, pp. 459–465, 7 2018.

[14] I. Oxyzoglou and I. Nerantzis, "Weight optimization of a f1 composite front wing," in *7th International Conference of BETA CAE Systems SA*, 06 2017.

[15] Z. Min, V. K. Kien, and L. J. Richard, "Aircraft morphing wing concepts with radical geometry change," *IES Journal Part A: Civil and Structural Engineering*, vol. 3, pp. 188–195, 2010.

[16] PPS, "Pressure profile systems." [Online]. Available: https://www.pressureprofile.com

[17] Scanivalve, "Scanivalve zoc 23b." [Online]. Available: https://scanivalve.com/products/pressure-measurement/miniature-analog-pressure-scanners/zoc23b-miniature-pressure-scanner/

[18] C. Norberg, "An experimental investigation of the flow around a circular cylinder: Influence of aspect ratio," *Journal of Fluid Mechanics*, vol. 258, pp. 287–316, 1994.

[19] J. Lee, S. Lee, and J. Cho, "Effect of inlet boundary layer suction on flow distortion in subsonic diffusing s-duct," *International Journal of Aeronautical and Space Sciences*, vol. 20, pp. 850–857, 2019.

[20] M. M. Wojewodka, C. White, S. Shahpar, and K. Kontis, "A review of flow control techniques and optimisation in s-shaped ducts," *International Journal of Heat and Fluid Flow*, vol. 74, pp. 223–235, 2018.

[21] S. Aslan and D. F. Kurtulus, "Numerical investigation of an s-duct diffuser at different inlet boundary conditions," *Advances in Sustainable Aviation*, pp. 111–128, 2017.

[22] T. Andreou, "Design optimisation and investigation into flow phenomena occurring in axial swirlers." 2022.

[23] L. Laser, "Litron ldy301 ylf." [Online]. Available: https://litron.co.uk/wp-content/uploads/2019/12/LitronLDY300PIV.pdf

[24] Photron, "Photron apx-rs." [Online]. Available: https://photron.com/applications_laser-illumination/

[25] Tokina, "Tokina lens." [Online]. Available: https://tokinalens.com/catalog/lenses/

[26] TSI, "Laserpulse synchronizer 610035." [Online]. Available: https://tsi.com/discontinued-products/laserpulse-synchronizer-610035/

[27] T. Endo and R. Himeno, "Direct numerical simulation of turbulent flow over a compliant surface," *Journal of Turbulence*, vol. 3, 2002.

[28] T. Suzuki, "Effects of a synthetic jet acting on a separated flow over a hump," *Journal of Fluid Mechanics*, vol. 547, pp. 331–359, 2006.

[29] J. A. Masad and V. Iyer, "Transition prediction and control in subsonic flow over a hump," *Physics of Fluids*, vol. 6, pp. 313–327, 1994.

[30] Siemens, "Simcenter star-ccm+ software." [Online]. Available: https://plm.sw.siemens.com/en-US/simcenter/fluids-thermal-simulation/star-ccm/

[31] D. Igali, O. Mukhmetov, Y. Zhao, S. C. Fok, and S. L. Teh, "Comparative analysis of turbulence models for automotive aerodynamic simulation and design," *International Journal of Automotive Technology*, vol. 20, pp. 1145–1152, 12 2019.

[32] N. Yan, X. Chen, and Y. Li, "Assessment of overturning risk of high-speed trains in strong crosswinds using spectral analysis approach," *Journal of Wind Engineering and Industrial Aerodynamics*, vol. 174, pp. 103–118, 3 2018.

[33] T. Li, D. Qin, and J. Zhang, "Effect of rans turbulence model on aerodynamic behavior of trains in crosswind," *Chinese Journal of Mechanical Engineering*, vol. 32, p. 85, 12 2019.

[34] J. Broniszewski and J. Piechna, "A fully coupled analysis of unsteady aerodynamics impact on vehicle dynamics during braking," *Engineering Applications of Computational Fluid Mechanics*, vol. 13, pp. 623–641, 2019.